

# Electronic Spin Transport in Dual-Gated Bilayer Graphene

Ahmet Avsar<sup>1\*</sup>, Ivan Jesus Vera-Marun<sup>2</sup>, Jun You Tan<sup>1</sup>, Gavin Kok Wai Koon<sup>1</sup>, Kenji Watanabe<sup>3</sup>,

Takashi Taniguchi<sup>3</sup>, Shaffique Adam<sup>1</sup> and Barbaros Özyilmaz<sup>1\*</sup>

**The elimination of extrinsic sources of spin relaxation is the key to the realization of the exceptional intrinsic spin transport performance of graphene. Towards this, we study charge and spin transport in bilayer graphene-based spin valve devices fabricated in a new device architecture that allows us to make a comparative study for separately investigating the roles of substrate and polymer residues on spin relaxation. The comparison between spin valves fabricated on SiO<sub>2</sub> and BN substrates suggests that substrate-related charged impurities, phonons and roughness do not limit the spin transport in current devices. On the other hand, the observation of a 5-fold enhancement in spin relaxation time in the encapsulated device highlights the significance of polymer residues on spin relaxation. We observe a spin relaxation length of ~10 μm in the encapsulated bilayer with a charge mobility of 24,000 cm<sup>2</sup>/Vs. The carrier density dependence of spin relaxation time has two distinct regimes;  $n < 4 \times 10^{12} \text{ cm}^{-2}$ , where spin relaxation time decreases monotonically as carrier concentration increases and  $n \geq 4 \times 10^{12} \text{ cm}^{-2}$ , where spin relaxation time exhibits a sudden increase. The sudden increase in the spin relaxation time with no corresponding signature in the charge transport suggests the observation of a magnetic resonance close to the charge neutrality point. We also demonstrate, for the first time, spin transport across bipolar p-n junctions in our dual-gated device architecture that fully integrates a sequence of encapsulated regions in its design. At low temperatures, strong suppression of spin signal was observed while a transport gap is induced, which is interpreted as a novel manifestation of impedance mismatch within the spin channel.**

<sup>1</sup>Centre for Advanced 2D Materials & Department of Physics, 2 Science Drive 3, National University of Singapore, Singapore 117542, Singapore, <sup>2</sup>The School of Physics and Astronomy, The University of Manchester, M139PL, Manchester, United Kingdom, <sup>3</sup>National Institute for Materials Science, 1-1 Namiki, Tsukuba 305-0044, Japan. Correspondence and requests for materials should be addressed to B. Ö. (email: [barbaros@nus.edu.sg](mailto:barbaros@nus.edu.sg)) and A. A. (email: [c2davsa@nus.edu.sg](mailto:c2davsa@nus.edu.sg))

## INTRODUCTION

Graphene is considered to be a promising spin channel material for future spintronics applications<sup>1</sup> due to its high electronic mobility<sup>2</sup>, weak spin orbit coupling<sup>3,4</sup> and negligible hyperfine interaction<sup>5,6</sup>. The initial spin transport studies were mainly performed in single layer<sup>7-10</sup> and bilayer exfoliated graphene<sup>9,11</sup> and large area graphene<sup>12-15</sup> deposited on conventional SiO<sub>2</sub> substrates. While enhanced spin relaxation times were reported for bilayer graphene-based devices compared to that in single layer, the relatively low spin diffusion constants overall yielded lower spin relaxation length of only 1-2  $\mu\text{m}$ <sup>9,11</sup>, far below the theoretical predictions<sup>16</sup>. One approach suggested for achieving longer distance spin communication is to increase the spin diffusion constants by fabricating higher mobility devices<sup>8,17</sup>.

For charge transport, it has already been shown that the carrier mobility of graphene devices on SiO<sub>2</sub> is mainly limited by interfacial charged impurities, surface roughness and phonons<sup>18-20</sup>. The demonstration of an order-of-magnitude improvement in the mobility of graphene encapsulated between atomically flat, charge trap free boron nitride crystals<sup>21,22</sup> has triggered the recent spin transport studies in encapsulated single layer graphene-based spin valves where a spin relaxation length up to  $\sim 12 \mu\text{m}$  has been observed<sup>23</sup>. For the case of bilayer graphene, the initial experiments on SiO<sub>2</sub> revealed an inverse scaling between spin and momentum relaxation times, e.g. the longest spin relaxation times were observed in the lowest mobility devices<sup>9,11</sup>. Within the standard picture of spin relaxation mechanism, such scaling was interpreted as the dominance of Dyakonov-Perel type scattering mechanism<sup>24</sup> in bilayer graphene-based spin valves on SiO<sub>2</sub>. Nevertheless, the strength of the extracted spin-orbit coupling was one order of magnitude higher than the theoretical predictions which brings into question this standard interpretation<sup>25</sup>. Recently, Kochan et al. proposed a new spin relaxation mechanism beyond the standard picture for both single layer and bilayer graphene driven by resonant scattering due to low concentration of magnetic impurities<sup>26,27</sup>. For the testing of this theory, bilayer graphene is a more ideal platform since a nonmonotonic correlation is predicted for the energy dependence of the spin relaxation time in bilayer graphene case that can be experimentally checked<sup>26</sup>.

Ultimately similar mobility enhancement in bilayer graphene may be a successful route to enhance the spin relaxation lengths, although this is strongly dependent on the scattering source and mechanism<sup>26,28–30</sup>.

## EXPERIMENTAL PROCEDURE

### Preparation of the devices

In this letter, we discuss the charge and spin transport in high mobility bilayer graphene-based spin valve devices, using a novel device architecture that overcomes the current technological limit of having a single encapsulated region<sup>23</sup>. In order to understand the effect of substrate and polymer residues on spin relaxation, we fabricated three types of bilayer graphene spin valve devices in a single sample; 1-) spin valve on SiO<sub>2</sub>, 2-) spin valve on BN, 3-) encapsulated spin valve between BN substrate and pre-patterned BN strip. The schematics for the fabrication of encapsulated spin valve devices are shown in Figure 1 a. The fabrication starts with the transfer of a bilayer graphene onto atomically flat BN crystals by utilizing the standard dry transfer method<sup>31</sup>. In order to create uniform and ultra clean interfaces, graphene on BN substrate is first etched with O<sub>2</sub> plasma into 1 μm width strip in the bubble and wrinkle free regions of the stack and then annealed at 340 °C for 6 hours under Ar/H<sub>2</sub> gaseous mixture (Figure 1b). This annealing process minimizes the fabrication residues formed during the etching processes. Meanwhile, a second BN layer is exfoliated onto SiO<sub>2</sub> (300 nm)/Si wafer, then patterned into BN strips by using e-beam lithography and etching (CHF<sub>3</sub>-O<sub>2</sub> (10-1 ratio) processes (Figure 1c). This pre-patterned BN layer, a novel aspect in our device architecture, is isolated from the wafer with a KOH etching process and finally transferred onto previously prepared BLG/BN stack as shown in Figure 1d. The final stack is annealed under same conditions as above. The fabrication is completed by forming MgO/Co/Ti (2.2 nm/30 nm/5nm) electrodes on top of both the h-BN strips and non-encapsulated regions of the graphene strip (Figure 1e). These electrodes serve as top gate electrodes and direct contact electrodes to bilayer graphene, respectively. The width of contact electrodes were varied from 300 nm to 1 μm in order to ensure the different coercive fields to switch the polarization directions of

ferromagnetic electrodes during spin transport measurements. The distance between edges of adjacent contacts is  $\sim 3 \mu\text{m}$  and the width of encapsulating BN strip is  $2.5 \mu\text{m}$ . The details for the fabrication of the MgO barrier layer are discussed in Supplementary Information. Even though the annealing process after metallization is a standard procedure to achieve very high mobilities in graphene-based heterostructure devices<sup>18,19</sup>, we skipped this process due to the degradation problem of ferromagnetic electrodes during annealing<sup>8</sup>. The pre-patterned top BN layer therefore adds a new degree of freedom to the device architecture, as it allows to easily design a series of encapsulated regions with arbitrary length, whereas the non-encapsulated regions destined for the contacts can be scaled down to the precision of the lithography technique. This represents a technological improvement to the prevalent approach in the literature, limited in practice to a single encapsulated region<sup>23</sup>.

### **Electrical measurements of the devices**

Measurements are carried out with standard ac lock-in techniques at low frequencies using the local four-terminal setup for charge transport measurements and the nonlocal setup for spin transport measurements (Figure 1 a). In the local charge transport measurements, the current flows between electrode 1 and electrode 4 and a local voltage drop is measured between electrode 2 and electrode 3. In the non-local measurement configuration, the current flows between the pair of electrode 1 (injector) and electrode 2, and a non-local voltage is recorded across the neighboring pair of electrode 3 (detector) and electrode 4.  $\text{SiO}_2$  and h-BN dielectrics are utilized to apply back and top gate biases ( $V_{\text{BG}}$  and  $V_{\text{TG}}$ ), respectively. Unless otherwise stated, electrode 6 is used to locally tune the carrier type and concentration (See Supplementary Information). All transport measurements are performed under vacuum conditions ( $\sim 1 \times 10^{-6}$  Torr). In this work, we have characterized a total number of 5 junctions in two separate samples (Sample A and B). The bilayer graphene in Sample A has both encapsulated and non-encapsulated junctions, allowing for a direct comparison of charge and spin transport for both cases (See Supplementary Information). Optical image of the completed Sample B is shown in Figure 1-e.

## RESULTS AND DISCUSSIONS

We first discuss the room temperature spin transport results of the non-encapsulated device in Sample A at  $V_{BG}=0V$ . The relative magnetization directions of the Co electrodes are being altered by sweeping the in-plane magnetic field along their easy axis. This changes the spin accumulation between the injector and detector electrodes, and hence leads to a nonlocal spin signal with a change in resistance of  $\Delta R \approx 0.3 \Omega$  (Figure 2a). We note that the observed spin signal is comparable to the earlier reports<sup>11,12,32</sup> (See Supplementary Information). In order to confirm the origin of the spin signal and extract the important spin parameters, we also performed Hanle spin precession measurements. For this purpose, the magnetization directions of the injector and detector electrodes are made parallel to each other by the application of an in-plane magnetic field. This is followed by the sweeping of a magnetic field perpendicular to the graphene plane forcing the spins to precess (Figure 2b). The obtained spin precession data is fitted with the solution of the Bloch equation,

$$R_{NL} \sim \int_0^{\infty} \frac{1}{\sqrt{4\pi D_S t}} \exp\left(\frac{-L^2}{4D_S t}\right) \exp\left(\frac{-t}{\tau_S}\right) \cos(\omega_L t) dt$$

where  $L \approx 1.7 \mu\text{m}$  being the separation between the electrodes (center-to-center distance) and  $\omega_L$  the Larmor frequency. This gives a spin relaxation time of  $\tau_S \approx 87 \text{ ps}$ , a spin diffusion constant of  $D_S \approx 0.02 \text{ m}^2/\text{s}$ , and hence, a spin relaxation length ( $\lambda_S = \sqrt{D_S \tau_S}$ ) of  $\lambda_S \approx 1.3 \mu\text{m}$ . Next, we characterize the adjacent, encapsulated device in the same sample. Clear spin valve and Hanle spin precession signals are obtained in this device as well (Figure 2-b&c). For this junction, we extracted a spin relaxation time  $\tau_S \approx 416 \text{ ps}$ , a spin diffusion constant of  $D_S \approx 0.089 \text{ m}^2/\text{s}$ , and, hence, a spin relaxation length of  $\lambda_S \approx 6.1 \mu\text{m}$  using the same fitting procedure as for the non-encapsulated junction. These measurements indicate four important conclusions: 1-) The extracted spin parameters in our non-encapsulated bilayer graphene are comparable to those extracted for bilayer devices on  $\text{SiO}_2$  with similar mobilities<sup>11</sup> (Inset Figure 2-d and See Supplementary Information). This suggests that substrate related issues such as roughness, interfacial charged impurities and surface phonons are not the limiting source for spin relaxation in current devices. 2-) Since the encapsulated region is protected against the polymer residues during the contact fabrication step, the 5-fold

enhancement of spin parameters in the encapsulated device compared to non-encapsulated one suggests that residues have a significant effect on spin transport. 3-) The observation of enhancement in the encapsulated device compared to the non-encapsulated one suggests that the contacts ( $\sim 5 \text{ k}\Omega$ ) are not the limiting factor for the spin relaxation. Note that the obtained spin parameters for the encapsulated device should be considered as lower bounds, since they will include also the spin transport in the non-encapsulated contact regions. Our observation now allows us to speculate that the observed long spin life times in ref. <sup>33</sup> could be attributed mainly to the polymer free fabrication of graphene spin valves rather than only improvement in contacts. This is also consistent with the observation of nearly 3-fold enhancement of up to 2.7 ns spin relaxation time in single layer graphene upon plasma hydrogenation treatment, even when supported on  $\text{SiO}_2$ , which could be partially attributed to the removal of such residues<sup>34</sup>.

Now we discuss the origin of the spin scattering mechanism in bilayer graphene. Figure 2-d shows the mobility dependence of spin relaxation time where we observe increase of spin relaxation time as the mobility increases. The increase of mobility is mainly achieved with decreasing the concentration of the impurity. The latter indicates that impurity scattering has a significant role in spin scattering, contrary to previous studies that have demonstrated that while charged impurities affect the carrier mobility they do not affect spin relaxation<sup>10,35,36</sup>. This suggests that while we are decreasing the concentration of charged impurity in our devices with the encapsulation process, we also unintentionally decrease the source of limiting spin scattering in the device. For instance this limiting source could be magnetic scatterers which have been recently predicted to increase the spin flipping process without having a significant influence on charge transport<sup>26,27</sup>. In order to check the role of the magnetic impurities on spin relaxation, we now investigate the carrier concentration dependence of local device resistance and spin relaxation times in both encapsulated and non-encapsulated devices.

Prior to the spin transport measurements, we first performed charge characterization of both encapsulated and non-encapsulated bilayer graphene junctions at room temperature. Our devices are

weakly electron doped, possibly due to a charge transfer process from MgO layer<sup>11,12</sup>. Mobilities of 3,600 cm<sup>2</sup>/Vs and 9,500 cm<sup>2</sup>/Vs are extracted at room temperature for the non-encapsulated and the encapsulated bilayer graphene, respectively by using  $R = \frac{L}{We\mu\sqrt{n_{res}^2+n^2}}$ . Here,  $\mu$  is the mobility,  $L$  and  $W$  are the length and width of channel,  $n$  is the charge carrier concentration and  $n_{res}$  is the residual concentration (See Supplementary Information)<sup>37</sup>. We first note that these room temperature mobilities are higher than the similar devices measured on SiO<sub>2</sub> (See ref. 9,11 and Supplementary Information), and consistent with previous works with spin-valve devices on BN where a final annealing step is not applied to keep the integrity of the spin polarized contacts<sup>8,23</sup>. It is also important to note that these mobilities are mainly limited by the residues formed during electrode fabrication process. However, the residual concentration is significantly reduced in the encapsulated junction ( $n_{res}=5.8\times10^{11}$  cm<sup>-2</sup>) compared to the non-encapsulated one ( $n_{res}=1.2\times10^{12}$  cm<sup>-2</sup>) since the top BN strip in the encapsulated device protects a large fraction of the junction against polymer contamination.

Figures 3-a&b show the carrier dependence of conductivity and spin relaxation time in the non-encapsulated and encapsulated junctions, respectively. We first discuss the low carrier concentration regime ( $n<4\times10^{12}$  cm<sup>-2</sup>), where most of the earlier spin transport measurements were performed. Here, spin relaxation time in the both the encapsulated and non-encapsulated devices has a monotonic dependence on carrier concentration. In the nonencapsulated junction, it decreases from 250 ps to 90 ps as electron carrier concentration is increased (Figure 3a). Similarly, a decrease from 330 ps to 260 ps is observed in the encapsulated junction as carrier concentration is increased in this low carrier concentration regime (Figure 3b). Such scaling is consistently observed in the all devices measured at both room temperature and 2.4K in this study (See Supplementary Information) and it is similar to what had previously been observed at low temperatures in lower mobility bilayer graphene spin valves on SiO<sub>2</sub> substrate<sup>9,11</sup>. Next, we discuss the spin relaxation times at high carrier concentration regime ( $n>4\times10^{12}$  cm<sup>-2</sup>). Around  $\sim 4\times10^{12}$  cm<sup>-2</sup>, we observe an upturn in the carrier concentration dependence of spin relaxation time in both encapsulated and non-encapsulated junctions (Coloured region in Figure

3a&b). Remarkably there is no corresponding signature in the charge transport at this carrier concentration regime. This previously unobserved upturn in the spin lifetime brings to question what is the dominant relaxation mechanism in bilayer graphene. The earlier experiments in bilayer graphene on  $\text{SiO}_2$  substrate have attributed the inverse scaling between spin and momentum relaxation times near  $\sim 2 \times 10^{12} \text{ cm}^{-2}$  to the presence of Dyakonov-Perel spin scattering mechanism<sup>11</sup>. This low density is below the regime where the upturn in spin relaxation time is observed and therefore the scaling at this point can lead to different conclusions. We first note that neither encapsulated nor nonencapsulated devices show an inverse relation between momentum and spin relaxation times at low carrier concentration regime as shown in Figure 3c&d. We also observe a clear increase of spin relaxation time as the mobility of the device increases (Figure 2d). All these indicate that Dyakonov-Perel spin relaxation is not the dominant mechanism in our devices. However at higher carrier concentration regime, spin and momentum relaxation times appear to change their dependence and scale inversely. Such dependence at both low and high carrier concentration regimes seem to agree with the recent theoretical work where spin relaxation in graphene is proposed to be dominated by resonant scatterers due to the presence of low concentration of magnetic impurities, such as polymer residues<sup>26</sup>. In that theory, the opposite carrier concentration dependence of spin relaxation in bilayer and single layer graphene was attributed to the different scales of energy fluctuations in these two systems due to their different density of states. Away from the puddle regime, the sudden increase of spin relaxation time at  $\sim 4-5 \times 10^{12} \text{ cm}^{-2}$  is expected for bilayer graphene due to the scattering from these resonant magnetic scatterers with no corresponding signature in the charge transport. We remark that, although our observations serve as an indication for the picture of resonant scattering mentioned above, there is no general agreement for the exact spin relaxation mechanism in bilayer graphene and further work is required to elucidate its complex nature.

Now, we turn our attention to the transport across p-n junctions in Sample B. The combination of local  $V_{TG}$  and global  $V_{BG}$  electrostatic gating allows us to locally control the charge density and type in the channel and create bipolar junctions in between injector and detector electrodes<sup>38</sup>. For this,  $V_{TG}$

was kept fixed at 0V, -2.5V and 2.5V while charge and spin transport were performed as a function of  $V_{BG}$ . We first discuss  $V_{TG}=0$  V case. Similar to the sample A, the device is slightly electron doped (Figure 4). The extracted electronic mobility is  $9,000 \text{ cm}^2/\text{Vs}$  at RT. Room temperature spin relaxation time and length at  $V_{BG} = 0$  V are 400 ps and  $5.75 \mu\text{m}$  respectively. Again, the spin relaxation time decreases as carrier concentration is increased. We observe clear pp'p and npn bipolar junctions while  $V_{BG}$  is swept at fixed  $V_{TG}= 2.5$  V and pp'p, pnp and nn'n bipolar junctions at  $V_{TG}= -2.5$  V. Conversely, the carrier concentration dependence of spin relaxation time has very similar behavior to the local device resistance, consistent with the response in the low carrier concentration regime discussed above, considering an effective averaging of the channel properties. At present we do not find strong evidence of significant spin scattering at the pn barriers.

Finally, we study the charge and spin transport at low temperature (2K). Presence of an on-site energy difference between the bottom and top layer induces a band gap in bilayer graphene<sup>39</sup>. This can be achieved with the application of a vertical electric field through the bilayer graphene plane. While infrared spectroscopy measurements yield large band gaps up to 250 meV<sup>40</sup>, the strong role played by disorder limits the expected strong suppression of charge transport measurements and results in only a few meV of effective transport gap<sup>41</sup>. Figure 5-a shows the 2D plot of local resistance as a function of  $V_{BG}$  and  $V_{TG}$ . Near the charge neutrality point, the device resistance increases  $\sim 5$ -fold as the total displacement electric field is increased. This is a direct indication of the induced transport gap<sup>39</sup>. The extracted electronic mobility is  $\sim 24,000 \text{ cm}^2/\text{Vs}$  at 2K. Next, we study spin transport near the charge neutrality point as the displacement field ( $D$ ) is increased in our dual-gated device. Figure 5-c&d show spin transport and spin precession measurements as  $D$  is increased. At  $D \sim 0$ , we calculate a spin relaxation length of  $\sim 9.5 \mu\text{m}$ . At very small  $D$ , we still observe a clear spin signal. The extracted spin relaxation times and lengths are in the order of  $\sim 500$  ps and  $\sim 10 \mu\text{m}$  respectively, similar to the  $D \sim 0$  case. This implies that no additional scattering happens at small gaps. However as  $D$  increases, we observe strong suppression of spin signal and eventually the signal becomes comparable to the noise

level ( $\sim 20$  m $\Omega$ ) and non-detectable. This prevents us extracting the spin relaxation times at large  $D$  values. Figure 5-b shows the sharp decrease in the spin signal as the local resistance at charge neutrality point increases. While a  $\Delta R_{NL} \sim R^{-1}$  dependence is expected for transparent (pin-hole) contacts in spin valve devices<sup>32</sup>, the observation of  $\Delta R_{NL} \sim R^{-3.04}$  dependence suggests the presence of an additional mechanism driving the decrease in nonlocal signal. This resulted in a modulation of more than one order of magnitude purely via electrostatic gating (Figure 5b). We attribute this dramatic response to the formation of a transport gap in the (encapsulated) dual-gated regions. The highly resistive state in those regions would effectively block the diffusion towards the nonlocal detector of the electronic spins, which will tend to remain within the (non-encapsulated) regions where the magnetic contacts are located. This scenario leads us to an interesting case of the spin conductivity mismatch problem<sup>42</sup>, where the regions with large and low spin conductance are both contained within the spin transport channel. We note that the spin signal at room temperature is modulated only by  $\sim 50\%$ , confirming the interpretation of a strong modulation only when a sizable transport gap is present. (See Supplementary Information).

## CONCLUSIONS

Here, we report spin transport in high mobility bilayer graphene spin valve devices encapsulated in BN. The effect of transport gap and p-n junctions on spin transport is discussed. Our comparative study suggests that substrate and contacts are not the key limiting factors for spin relaxations but rather pinpoint the role of polymer residues or ambient adsorbates. We achieve spin relaxation lengths of  $\sim 6$   $\mu\text{m}$  and  $\sim 10$   $\mu\text{m}$  at RT and 2K, respectively. The carrier concentration dependence of spin relaxation time seems to be in good agreement with the resonant scattering-based spin scattering theory. Our flexible device architecture offers the prospect of further enhancement of the extracted spin transport parameters, by allowing optimization of the length of the encapsulated and the contact regions.

## CONFLICT OF INTEREST

The authors declare no conflict of interest.

## ACKNOWLEDGEMENTS

B. Ö. would like to acknowledge support by the National Research Foundation, Prime Minister's Office, the Singapore under its Competitive Research Programme (CRP Award No. NRF-CRP9-2011-3), the Singapore National Research Foundation Fellowship award (RF2008-07), and the SMF-NUS Research Horizons Award 2009-Phase II.

## AUTHOR CONTRIBUTIONS

A.A., I.J.V.M. and B.Ö. designed the experiments. A.A., J.Y.T. and G. K. K. W. fabricated the samples. A.A. performed transport measurements and analyzed the data. K.W. and T. T. grew the hBN crystals. A.A., I.J.V.M., S.A. and B.Ö. discussed the results and wrote the manuscript.

## REFERENCES

1. Han, W., Kawakami, R. K., Gmitra, M. & Fabian, J. Graphene spintronics. *Nat. Nanotechnol.* **9**, 794–807 (2014).
2. Geim, A. K. Graphene: status and prospects. *Science* **324**, 1530–4 (2009).
3. Konschuh, S., Gmitra, M. & Fabian, J. Tight-binding theory of the spin-orbit coupling in graphene. *Phys. Rev. B* **82**, 245412 (2010).
4. Huertas-Hernando, D., Guinea, F. & Brataas, A. Spin-orbit coupling in curved graphene, fullerenes, nanotubes, and nanotube caps. *Phys. Rev. B* **74**, 155426 (2006).
5. Trauzettel, B., Bulaev, D. V., Loss, D. & Burkard, G. Spin qubits in graphene quantum dots. *Nat. Phys.* **3**, 192–196 (2007).
6. Wojtaszek, M., Vera-Marun, I. J., Whiteway, E., Hilke, M. & van Wees, B. J. Absence of hyperfine effects in <sup>13</sup>C-graphene spin-valve devices. *Phys. Rev. B* **89**, 035417 (2014).
7. Tombros, N., Jozsa, C., Popinciuc, M., Jonkman, H. T. & van Wees, B. J. Electronic spin transport and spin precession in single graphene layers at room temperature. *Nature* **448**, 571–4 (2007).
8. Zomer, P. J., Guimarães, M. H. D., Tombros, N. & van Wees, B. J. Long-distance spin transport in high-mobility graphene on hexagonal boron nitride. *Phys. Rev. B* **86**, 161416 (2012).

9. Han, W. & Kawakami, R. K. Spin Relaxation in Single-Layer and Bilayer Graphene. *Phys. Rev. Lett.* **107**, 047207 (2011).
10. Pi, K. *et al.* Manipulation of Spin Transport in Graphene by Surface Chemical Doping. *Phys. Rev. Lett.* **104**, 187201 (2010).
11. Yang, T.-Y. *et al.* Observation of Long Spin-Relaxation Times in Bilayer Graphene at Room Temperature. *Phys. Rev. Lett.* **107**, 047206 (2011).
12. Avsar, A. *et al.* Toward wafer scale fabrication of graphene based spin valve devices. *Nano Lett.* **11**, 2363–8 (2011).
13. Maassen, T. *et al.* Long spin relaxation times in wafer scale epitaxial graphene on SiC(0001). *Nano Lett.* **12**, 1498–502 (2012).
14. Dlubak, B. *et al.* Highly efficient spin transport in epitaxial graphene on SiC. *Nat. Phys.* **8**, 557–561 (2012).
15. Kamalakar, M. V., Groenveld, C., Dankert, A. & Dash, S. P. Long distance spin communication in chemical vapour deposited graphene. *Nat. Commun.* **6**, 6766 (2015).
16. Ertler, C., Konschuh, S., Gmitra, M. & Fabian, J. Electron spin relaxation in graphene: The role of the substrate. *Phys. Rev. B* **80**, 041405 (2009).
17. Guimarães, M. H. D. *et al.* Spin transport in high-quality suspended graphene devices. *Nano Lett.* **12**, 3512–7 (2012).
18. Dean, C. R. *et al.* Boron nitride substrates for high-quality graphene electronics. *Nat. Nanotechnol.* **5**, 722–6 (2010).
19. Tan, J. Y. *et al.* Electronic transport in graphene-based heterostructures. *Appl. Phys. Lett.* **104**, 183504 (2014).
20. Zomer, P. J., Dash, S. P., Tombros, N. & van Wees, B. J. A transfer technique for high mobility graphene devices on commercially available hexagonal boron nitride. *Appl. Phys. Lett.* **99**, 232104 (2011).
21. Mayorov, A. S. *et al.* Micrometer-scale ballistic transport in encapsulated graphene at room temperature. *Nano Lett.* **11**, 2396–9 (2011).
22. Wang, L. *et al.* One-dimensional electrical contact to a two-dimensional material. *Science* **342**, 614–7 (2013).
23. Guimarães, M. H. D. *et al.* Controlling Spin Relaxation in Hexagonal BN-Encapsulated Graphene with a Transverse Electric Field. *Phys. Rev. Lett.* **113**, 086602 (2014).
24. Dyakonov, M. & Perel, V. Spin relaxation of conduction electrons in noncentrosymmetric semiconductors. *Sov. Phys. Solid State*, **13**, 3023 (1972).
25. Konschuh, S., Gmitra, M., Kochan, D. & Fabian, J. Theory of spin-orbit coupling in bilayer graphene. *Phys. Rev. B* **85**, 115423 (2012).

26. Kochan, D., Irmer, S., Gmitra, M. & Fabian, J. Theory of spin-relaxation in bilayer graphene: resonant scattering by magnetic impurities. arXiv:1504.03898 (2015).
27. Kochan, D., Gmitra, M. & Fabian, J. Spin Relaxation Mechanism in Graphene: Resonant Scattering by Magnetic Impurities. *Phys. Rev. Lett.* **112**, 116602 (2014).
28. Tuan, D. Van, Ortmann, F., Soriano, D., Valenzuela, S. O. & Roche, S. Pseudospin-driven spin relaxation mechanism in graphene. *Nat. Phys.* **10**, 857–863 (2014).
29. Castro Neto, A. & Guinea, F. Impurity-Induced Spin-Orbit Coupling in Graphene. *Phys. Rev. Lett.* **103**, 026804 (2009).
30. Van Tuan, D., Ortmann, F., Cummings, A. W., Soriano, D. & Roche, S. Spin Dynamics and Relaxation in Graphene Dictated by Electron-hole Puddles. arXiv:1509.07949, (2015).
31. Avsar, A. *et al.* Spin-orbit proximity effect in graphene. *Nat. Commun.* **5**, 4875 (2014).
32. Han, W.; Pi, K.; McCreary, K. M.; Li, Y.; Wang, J. J. I.; Swartz, A. G.; Kawakami, R. K. Tunneling Spin Injection into Single Layer Graphene *Phys. Rev. Lett.* **105**, 167202 (2010).
33. Drögeler, M. *et al.* Nanosecond spin lifetimes in single- and few-layer graphene-hBN heterostructures at room temperature. *Nano Lett.* **14**, 6050–5 (2014).
34. Wojtaszek, M., Vera-Marun, I. J., Maassen, T. & van Wees, B. J. Enhancement of spin relaxation time in hydrogenated graphene spin-valve devices. *Phys. Rev. B* **87**, 081402 (2013).
35. Han, W. *et al.* Spin relaxation in single-layer graphene with tunable mobility. *Nano Lett.* **12**, 3443–7 (2012).
36. Lundeberg, M. B., Yang, R., Renard, J. & Folk, J. A. Defect-Mediated Spin Relaxation and Dephasing in Graphene. *Phys. Rev. Lett.* **110**, 156601 (2013).
37. Kim, S. *et al.* Realization of a high mobility dual-gated graphene field-effect transistor with Al<sub>2</sub>O<sub>3</sub> dielectric. *Appl. Phys. Lett.* **94**, 062107 (2009).
38. Özyilmaz, B. *et al.* Electronic Transport and Quantum Hall Effect in Bipolar Graphene p – n – p Junctions. *Phys. Rev. Lett.* **99**, 166804 (2007).
39. Oostinga, J. B., Heersche, H. B., Liu, X., Morpurgo, A. F. & Vandersypen, L. M. K. Gate-induced insulating state in bilayer graphene devices. *Nat. Mater.* **7**, 151–7 (2008).
40. Zhang, Y. *et al.* Direct observation of a widely tunable bandgap in bilayer graphene. *Nature* **459**, 820–3 (2009).
41. Taychatanapat, T. & Jarillo-Herrero, P. Electronic Transport in Dual-Gated Bilayer Graphene at Large Displacement Fields. *Phys. Rev. Lett.* **105**, 166601 (2010).
42. Maassen, T., Vera-Marun, I. J., Guimarães, M. H. D. & van Wees, B. J. Contact-induced spin relaxation in Hanle spin precession measurements. *Phys. Rev. B* **86**, 235408 (2012).

(43) Inglá-Aynés, J.; Guimaraes, M. H. D.; Meijerink, R. J.; Zomer, P. J.; Wees, B. J. Van.arXiv:1506.00472, **2015**.

## Notes

During the preparation of this manuscript, we became aware of related works on the spin transport in dual-gated bilayer graphene spin valves<sup>43</sup>.

## FIGURE CAPTIONS

**Figure 1 | Device Characterization.** (a) Schematics of the device fabrication. (b) Bilayer graphene is first transferred on top of BN layer and this step is followed by etching of graphene into a strip. (c) Then, a second BN layer is exfoliated onto standard wafer and etched into strips. (d) Then, a final transfer is done to encapsulate the bilayer graphene on BN with the pre-patterned BN. The image is captured after the spin coating with PMMA to enhance the contrast of graphene. (e) Finally ferromagnetic contacts are deposited under ultra high vacuum conditions.

**Figure 2 | Electronic spin transport measurement at gate voltage = 0V.** (a-b) Spin transport and spin precession measurements in bilayer graphene on BN substrate. (b-c) Spin transport and spin precession measurements in encapsulated bilayer graphene. The measurements are conducted at room temperature. (d) Room temperature carrier mobility dependence of spin relaxation time.

**Figure 3 | Gate dependent electronic spin transport measurement.** (a-b) Carrier concentration dependence of spin relaxation times for bilayer graphene on BN and encapsulated bilayer graphene spin valves. Non-encapsulated device is measured at 2.4 K and encapsulated device is measured at room temperature by varying the  $V_{TG}$  while  $V_{BG}$  is fixed at 25V. The dotted lines in the bottom panels are guide the eye, showing the expected spin relaxation times without involving the effect of magnetic resonance. (c-d) Comparison between spin and momentum scattering times for the devices shown in Figure 3 a&b. Cyan color points represent the high carrier regime.

**Figure 4 | Bipolar electronic spin transport measurement.**  $V_{BG}$  dependence of device resistance and spin relaxation time at fixed, small  $V_{TG}$  values.

**Figure 5 | Electronic spin transport measurement in the presence of band gap.** (a) 2D color plot of local device resistance as a function of top and back gate voltage. Device resistance at Dirac point shows 5-fold increase due to opening a band gap. (b) Spin signal diminishes very rapidly as the transport gap is increased. Black line shows the fitting line. (c&d) Spin transport and spin precession measurements along minimum carrier concentration. The measurement points are highlighted in 2D color plot with their corresponding colors.

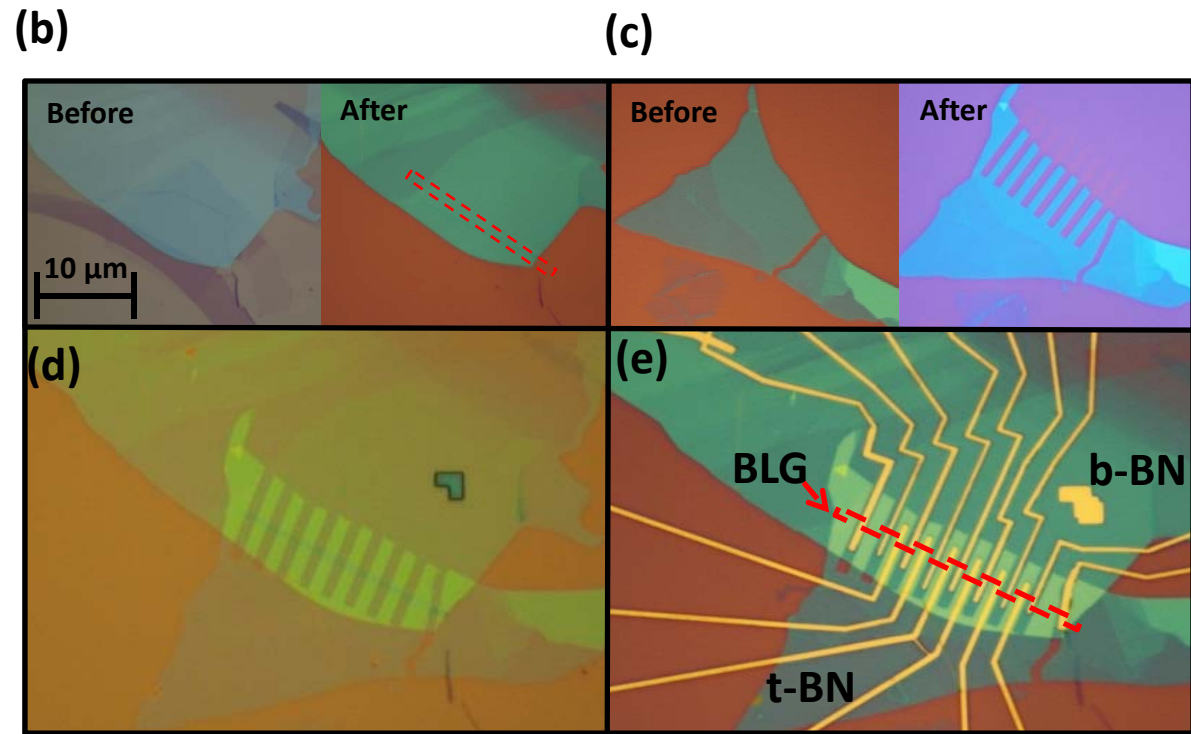
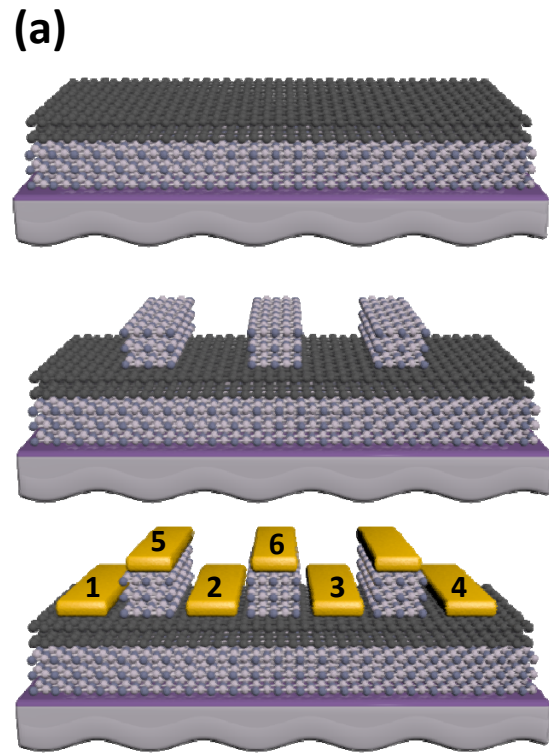
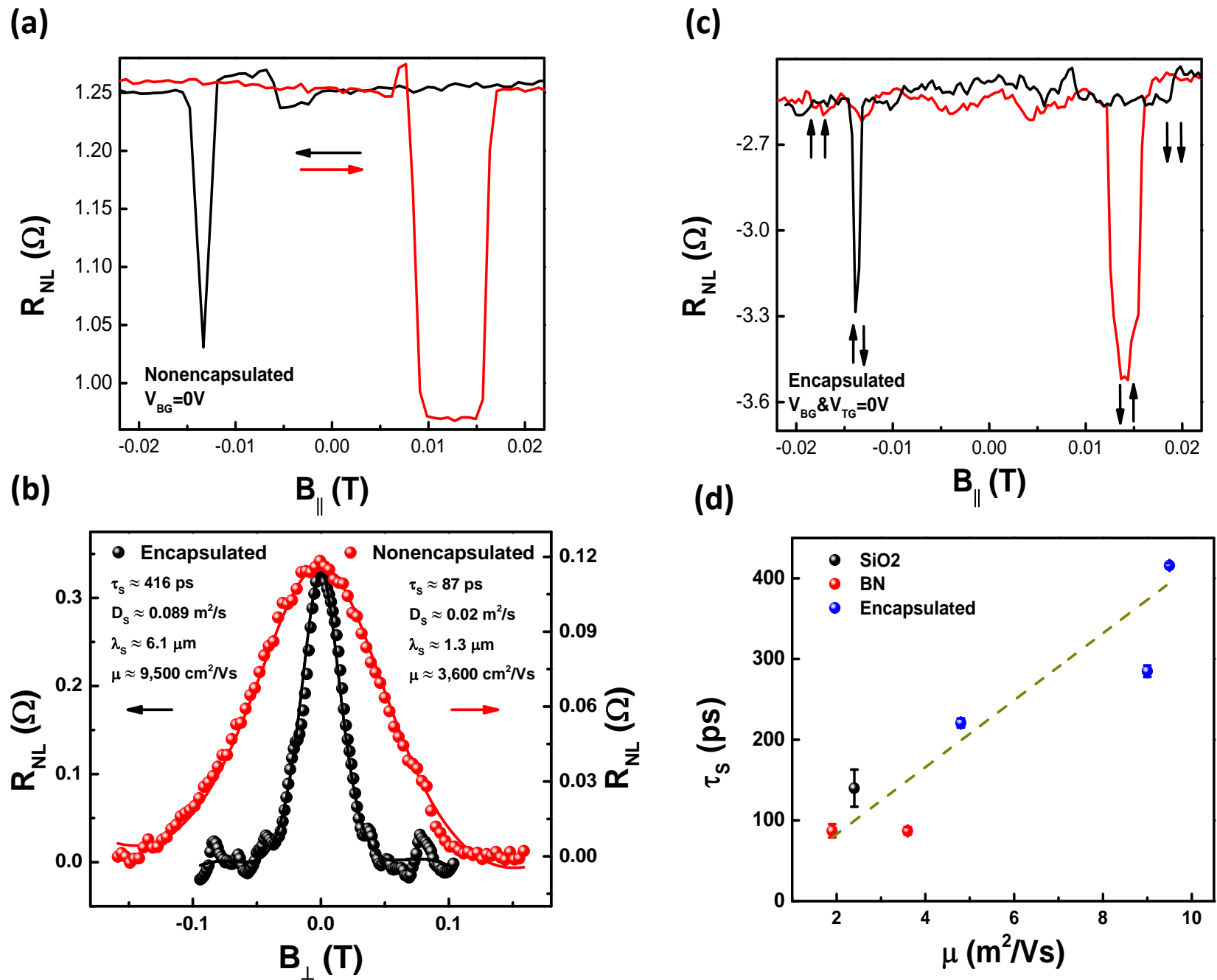
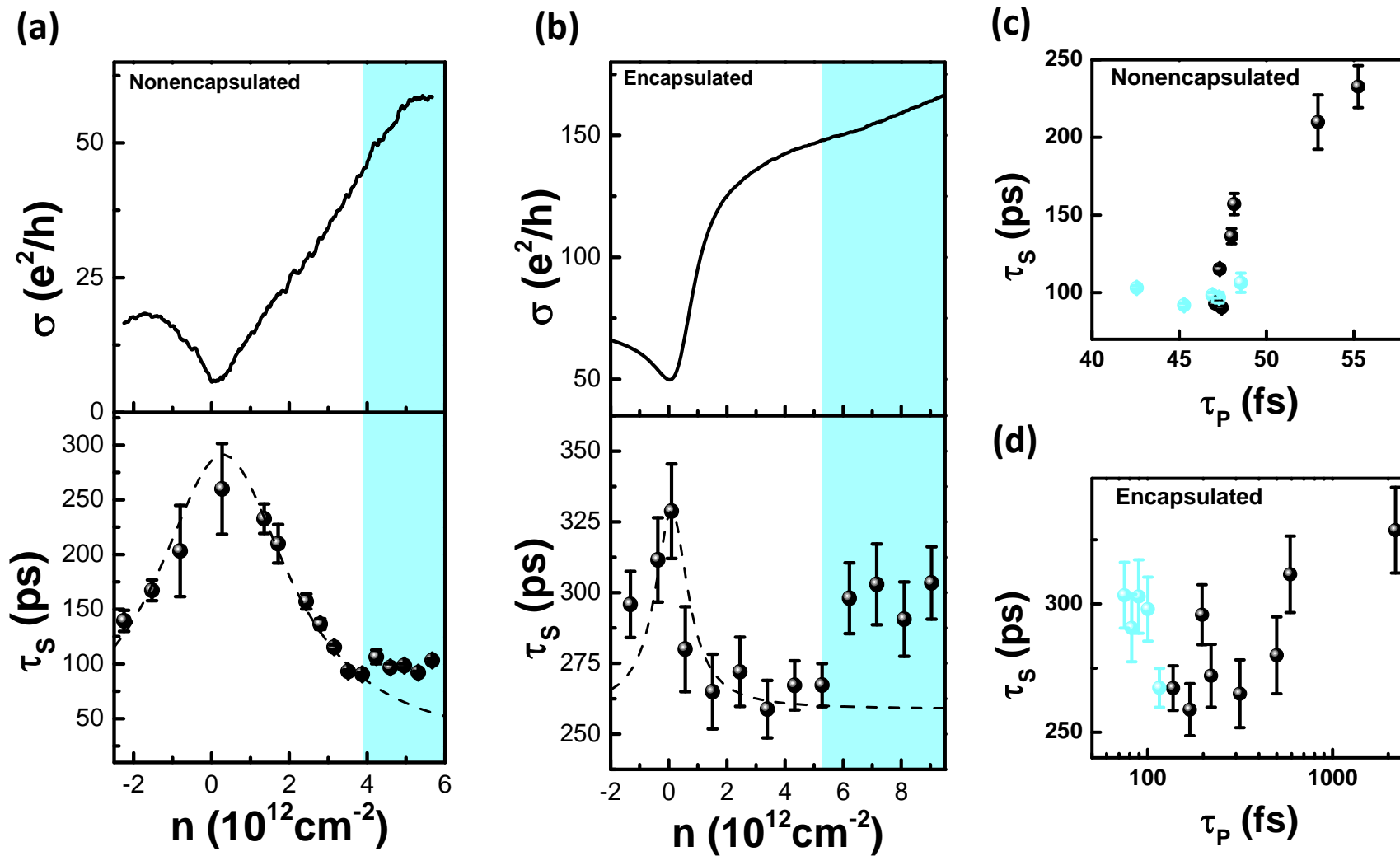


Figure 1



**Figure 2**



**Figure 3**

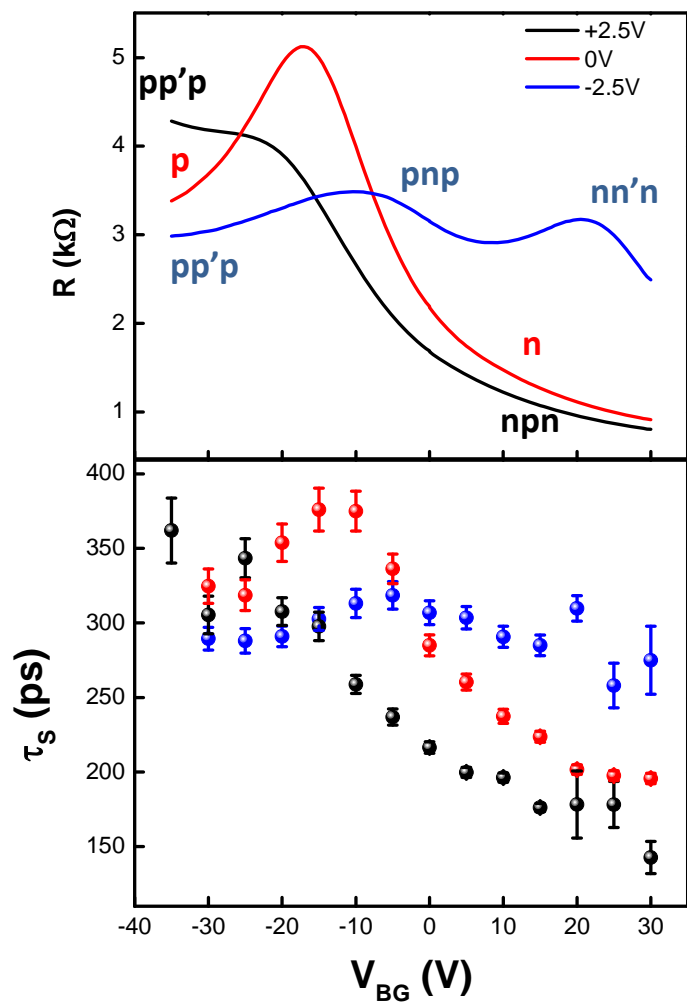


**Figure 4**

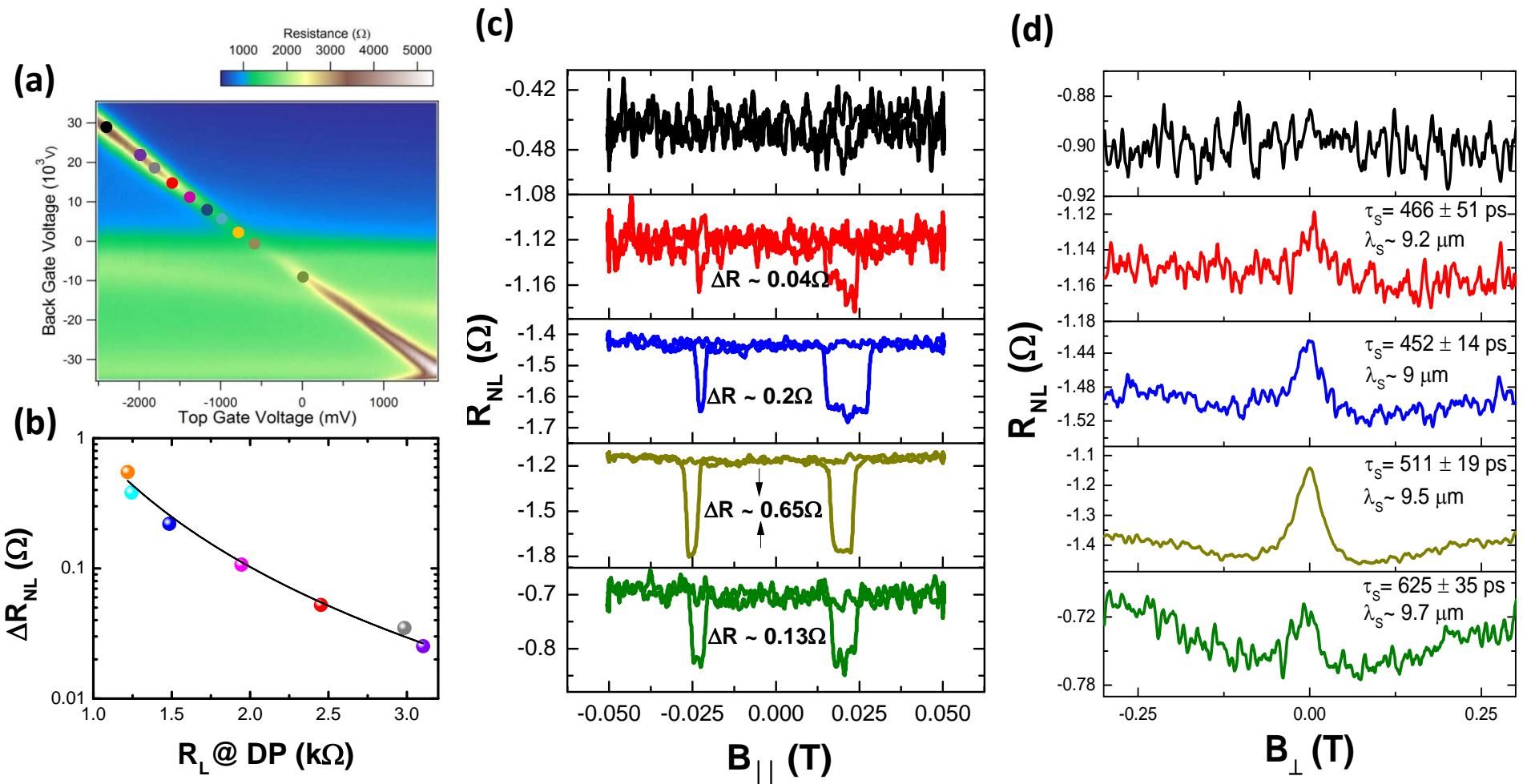


**Figure 5**